

## Chapter 2

# Structural Characterization

**Abstract** The experimentally fabricated GO powders are usually water dispersible, insulating, and light brown in color. After the experimental synthesis, one important issue is to determine the structure of GO. So far, the structure of GO is still ambiguous due to its nonstoichiometry since the types of oxygen-containing groups and their arrangements across the carbon network vary substantially under different synthesis conditions. Generally, to determine the structure of GO, some primary questions have to be illuminated: (1) Which functional groups are present? (2) What are the amount and relative fraction of the functional groups? (3) How do these functional groups distribute spatially over the graphene plane? (4) How do the amount and distribution of these groups evolve during reduction? Spectroscopic techniques, such as solid-state nuclear magnetic resonance (NMR), X-ray photoelectron spectroscopy (XPS), X-ray absorption near-edge spectroscopy (XANES), Fourier transform infrared spectroscopy (FT-IR) and Raman spectroscopy, can provide essential insights into the types of oxygenated functional groups in GO and their distributions. Besides, microscopic techniques including transmission electron microscopy (TEM), scanning tunneling microscopy (STM), atomic force microscopy (AFM), and scanning transmission electron microscopy (STEM) have also been used to determine the atomic structures of GO.

## 2.1 Spectroscopic Characterization

### 2.1.1 Solid-State NMR

The solid-state NMR spectra of different GO samples exhibit similar resonance patterns featuring three peaks at 60, 70 and 130 ppm and their relative intensities do not change significantly upon oxidation. In 1996, Klinowski's group [1] studied the structure of GO by using the  $^{13}\text{C}$  and  $^1\text{H}$  NMR spectra and assigned the 60 ppm peak to hydroxyl ( $\text{C}-\text{OH}$ ), the 70 ppm peak to epoxide ( $\text{C}-\text{O}-\text{C}$ ), and the 130 ppm one to non-aromatic carbon double bonds ( $>\text{C}=\text{C}<$ ). However, the identification

of the first two peaks at 60 and 70 ppm was uncertain due to lacking of sufficient spectral information. Then, in 1997 and 1998, the same group revisited the structure of GO and critically assigned the peak around 60 ppm to epoxide (C–O–C), the peak around 70 ppm to hydroxyl (C–OH), and the peak around 130 ppm to non-aromatic carbon double bonds ( $>C=C<$ ) [2, 3]. Afterwards, Szabó et al. [4] also examined the structure of GO by the  $^{13}\text{C}$  NMR spectra and obtained two featured signals at 57.6 and 69.2 ppm, which corresponds to the epoxide (C–O–C) and hydroxyl (C–OH), respectively. In addition, they found two other peaks at 92.9 and 166.3 ppm as well, but were not able to clearly assign them to any specific groups.

A more accurate NMR characterization of GO was fulfilled in 2008 by Cai et al. [5] using high-resolution solid-state NMR with magic angle spinning (MAS). It was confirmed that the peak around 60 ppm corresponds to epoxide, the peak around 70 ppm corresponds to hydroxyl, and the peak around 130 ppm corresponds to  $\text{sp}^2$  carbon. Until then, the three major chemical shift peaks around 60, 70, and 130 ppm are commonly accepted and assigned to epoxy, hydroxyl and graphitic  $\text{sp}^2$  carbon, respectively. As a consequence, epoxy and hydroxyl are determined as the two major functional groups across the basal plane of GO. In addition, in the high-resolution  $^{13}\text{C}$  NMR spectra [4–6], the other three minor peaks at about 101, 167, and 191 ppm were also found, which were tentatively assigned to lactol, ester carbonyl and ketone groups, respectively. In 2009, Gao et al. [7] further assigned the peak around 101 ppm to five- or six-membered-ring lactol decorated on the edge of holes in GO flakes.

A recent study by Zhang et al. [8] labeled all the six peaks mentioned above, where peaks at 61, 70, 101, 130, 169 and 193 ppm were assigned to groups of C–O–C, C–OH, O–C–O, graphitic  $\text{sp}^2$  C, O=C–O, and C=O, separately. To gain information about the distribution of major functional groups, two- and multi-dimensional NMR spectra conducted by Ruoff's group [5, 9] revealed that epoxide and hydroxyl were close to each other, with some tiny islands of pure epoxies or hydroxyls. Diagonal signals eliminated in the two-dimensional double-quantum/single-quantum spectrum shows that the cross peak of epoxide is at  $(\omega_{\text{SQ}}, \omega_{\text{DQ}}) = (60, 130 \text{ ppm})$  and the cross peak of hydroxyl is at  $(\omega_{\text{SQ}}, \omega_{\text{DQ}}) = (70, 130 \text{ ppm})$ , respectively [9]. This confirms clearly that the epoxide and hydroxyl carbons are directly bonded. Besides, the major peaks (60 and 70 ppm) in the NMR spectra were related to the carbon atoms single-bonded to oxygen atoms. Figure 2.1 gives the typical  $^{13}\text{C}$  NMR spectra of GO.

### 2.1.2 XPS

As a complementarity to the NMR spectra, XPS can further unveil the nature of carbon atoms in different chemical environments. Comparing the survey scan spectra of bare graphite and GO [4], it was found that the C and O atoms were presented at the surface of both systems; but the oxygen content of GOs

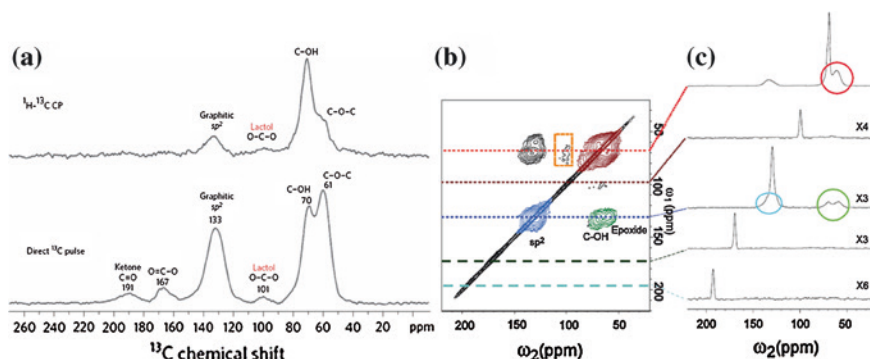


**Fig. 2.1** **a**  $^1\text{H}$ - $^{13}\text{C}$  cross polarization (CP) spectrum of GO obtained with 7.6 kHz MAS and a contact time of 1 ms (67,000 scans), and a direct  $^{13}\text{C}$  pulse spectrum obtained with 12 kHz MAS and a  $90^\circ$   $^{13}\text{C}$  pulse (10,000 scans). Reprinted with permission from Ref. [7]. Copyright (2009) Nature Publishing Group. **b** 2D  $^{13}\text{C}/^{13}\text{C}$  chemical-shift correlation solid-state NMR spectra of GO; **c** slices selected from the 2D spectrum at the indicated positions (70, 101, 130, 169, and 193 ppm) in the  $\omega_1$  dimension. Reprinted with permission from Ref. [5]. Copyright (2008) American Association for the Advancement of Science

was much higher because of the oxidative treatment, as shown in Fig. 2.2a, b. Further high-resolution XPS spectra demonstrated that in the C 1s signal of pristine GO, there are five different chemically shifted components at 284.5, 285.86, 286.55, 287.5 and 289.2 eV respectively, which can be assigned to  $\text{sp}^2$  carbon atoms in aromatic rings (284.5 eV) and C atoms bonded to hydroxyl (C-OH, 285.86 eV), epoxy (C-O-C, 286.55 eV), carbonyl ( $>\text{C}=\text{O}$ , 287.5 eV), and carboxyl groups (COOH, 289.2 eV), respectively [10–13], as shown in Fig. 2.2c. However, the presence of carbonyl ( $>\text{C}=\text{O}$ ) groups is still ambiguous. Some reports [3, 14] only considered four feature components of the deconvolution of the C 1s spectra by ignoring the presence of  $>\text{C}=\text{O}$  groups, i.e.  $\text{sp}^2$  carbons, C-OH, C-O-C, and COOH. Further information provided by the O 1s spectra can complement the information from the C 1s spectra. Deconvolution of the O 1s spectra indicates three main peaks around 531.08, 532.03, and 533.43 eV, which were assigned to C=O (oxygen doubly bonded to aromatic carbon) [10, 15], C-O (oxygen singly bonded to aliphatic carbon) [16, 17], and phenolic (oxygen singly bonded to aromatic carbon) [16, 17] groups, respectively, as shown in Fig. 2.2d. On the other hand, the pristine GO shows an additional peak at a higher binding energy (534.7 eV) [12], which originates from the chemisorbed/intercalated adsorbed water molecules.

An important parameter that can be used to characterize the degree of oxidation in GO is the fraction of  $\text{sp}^2$  carbon, which can be estimated by dividing the area under the  $\text{sp}^2$  peak by the area of C 1s peak. In pristine GO, the fraction of  $\text{sp}^2$  carbons is only ~40 %. During thermal reduction, the amount of  $\text{sp}^2$  carbons gradually increases due to the loss of oxygen. It reaches a maximum value of ~80 % at

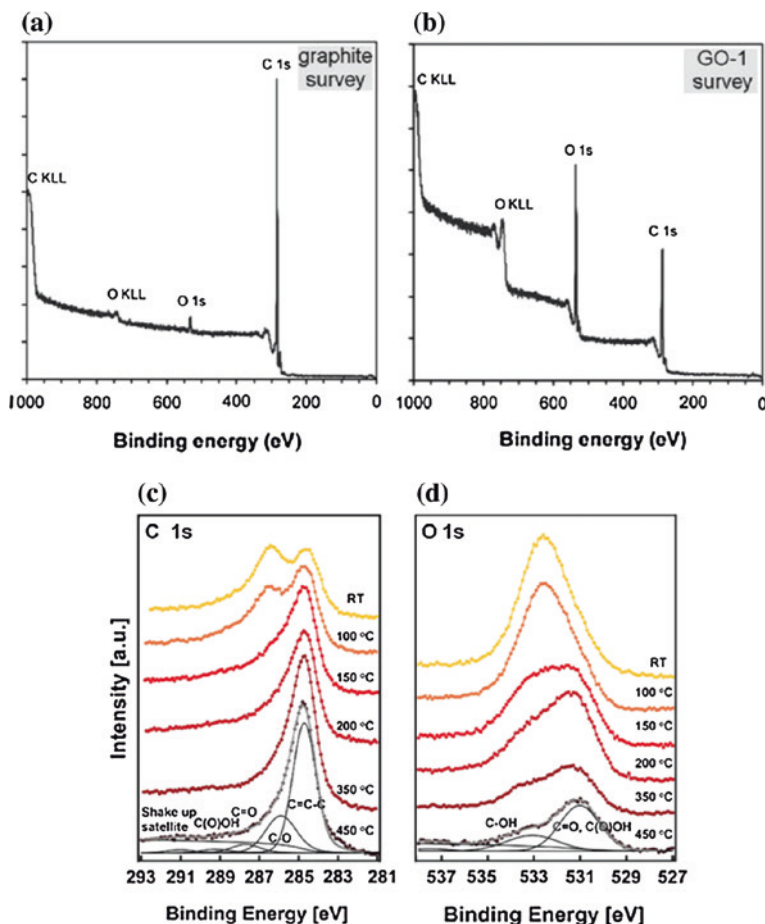


**Fig. 2.2** a, b are XPS spectra of graphite and GO separately. Reprinted with permission from Ref. [4]. Copyright (2006) American Chemical Society. c, d are high-resolution XPS spectra of the C 1s and O 1s signals in GO. Reprinted with permission from Ref. [10]. Copyright (2009) WILEY-VCH Verlag GmbH & Co. KGaA, Weinheim

an oxygen content of  $\sim 8$  atom% (C/O ratio 12.5:1) [10, 17]. This suggests that the remaining oxygen is responsible for  $\sim 20$  % of the  $sp^3$  bonding.

In addition, XPS can further elucidate change of the functional groups of GO at different degrees of oxidation [18]. At the initial stage, during increasing the oxidation level, intensity of the C–OH and –O–C=O functional groups increases and the corresponding intensity of C–C decreases. In the following, further increase of the oxidation results in the formation of epoxide groups along with the hydroxyl and carboxyl groups. Afterwards, continually oxidizing GO will enhance the intensity of epoxide groups but reduce the intensity of hydroxyl and carboxyl groups simultaneously.

### 2.1.3 XANES

XANES is another powerful tool for characterizing the GO materials. It provides information on degree of bond hybridization in mixed  $sp^2/sp^3$  bonded carbon, specific bonding configurations of functional atoms, and degree of alignment of the graphitic crystal structures within GO [19]. As shown in Fig. 2.3a, the high-resolution C K-edge XANES spectrum of GO demonstrates distinctive unoccupied  $\pi^*$  and  $\sigma^*$  states around 285.2 and 293.03 eV, respectively, which can be primarily assigned to the  $1s \rightarrow \pi^*$  and  $1s \rightarrow \sigma^*$  transitions in the graphitic carbon atoms [13, 20]. Meanwhile, there is a broadening of the absorption peak at 289.3 eV, corresponding to the  $1s \rightarrow \pi^*$  transitions in the carbon atoms bonded with the oxygen atoms. The ratio of  $\pi^*/\sigma^*$  peaks at the C K-edge can be used to estimate the relative concentration of  $sp^2$  domain configurations in an  $sp^3$  matrix of GO, where carbon atoms are attached to oxygen groups. Thus, this ratio gives the degree of oxidation in GO [13].

On the other hand, the O K-edge XANES spectrum of GO [13, 21] generally shows several distinct absorption peaks at 531.5, 534.0, 535.5, 540.0, 542.0, and 544.5 eV, respectively, as presented in Fig. 2.3b. These peaks have been separately assigned to  $\pi^*(C=O)$ ,  $\pi^*(C-O)$ ,  $\sigma^*(O-H)$ ,  $\sigma^*(C-O)$ ,  $\sigma^*(C=O)$ , and  $\sigma^*(C=O)$  [21]. Therefore, the O K-edge spectrum further helps to realize the GO structure, which clarifies the chemical composition of the oxygen-containing groups. According to Pacilé et al.'s measurements [21], the groups of epoxy, hydroxyl and carbonyl are likely to be attached to aromatic rings, while the carboxyl groups are likely to be bonded to the edges of the GO sheets.

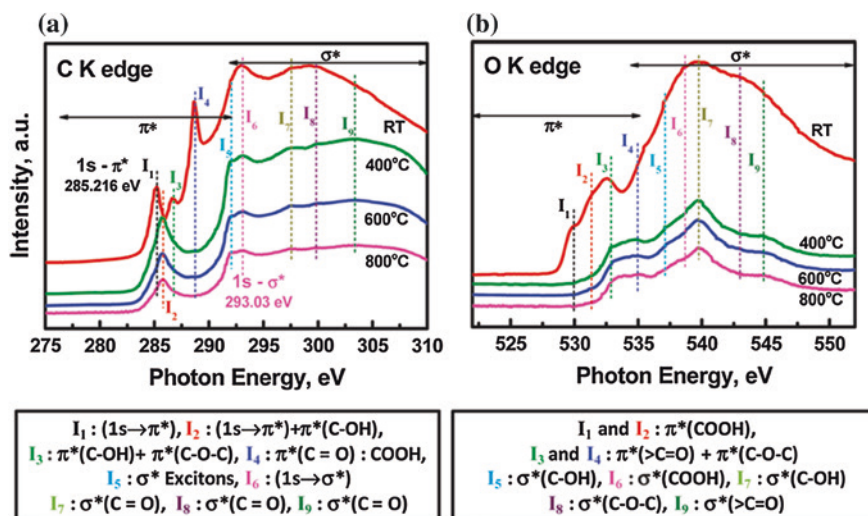


**Fig. 2.3** High-resolution **a** C K-edge and **b** O K-edge synchrotron NEXAFS spectra at different reduction temperatures. The spectra were shifted in y-scale for clarity. Reprinted with permission from Ref. [13]. Copyright (2011) American Chemical Society

### 2.1.4 FT-IR

FT-IR spectroscopy is recognized as an important tool to study different types of functional groups. From the FT-IR characterization, Lee et al. [22] found that there are four main peaks in the FT-IR spectra of GO, as described detailedly in the following. Firstly, the peak at  $1,050\text{ cm}^{-1}$  arises from epoxide groups (C–O–C). Secondly, the one centered at  $1,680\text{ cm}^{-1}$  corresponds to the vibrational mode of the ketone groups (C=O). Another peak at  $1,380\text{ cm}^{-1}$  is assigned to a C–O vibrational mode. Finally, the peak at  $3,470\text{ cm}^{-1}$  denotes C–OH stretching.

Bagri et al. [15] studied the structural evolution of GO during reduction. At the initial stage where GO is mildly annealed at 423 K, the FT-IR characterization shows that pristine GO was composed of hydroxyls ( $3,050\text{--}3,800\text{ cm}^{-1}$ ), carbonyls ( $1,750\text{--}1,850\text{ cm}^{-1}$ ), carboxyls ( $1,650\text{--}1,750\text{ cm}^{-1}$ ), C=C ( $1,500\text{--}1,600\text{ cm}^{-1}$ ) and ethers and/or epoxides ( $1,000\text{--}1,280\text{ cm}^{-1}$ ), as displayed in part (1) of Fig. 2.4a. After annealing to 448 K for 5 min, the FT-IR spectrum changes, indicating that the carboxyl groups are removed, as shown in part (2) of Fig. 2.4a. When further annealing to 1,023 K, hydroxyls disappear continuously and some ether groups are formed, as displayed in part (3) of Fig. 2.4a. In fact, the hydroxyls are not detected in infrared spectra at temperature above 773 K.

Similarly, Krishnamoorthy et al. [18] also investigated the structure of GO with different degrees of oxidation using FT-IR spectroscopy, as presented in Fig. 2.4b. The  $\text{sp}^2/\text{sp}^3$  ratios of GO samples from S-1 to S-6 are 2.15, 1.52, 0.36, 0.31, 0.27, and 0.25, respectively. The FT-IR show band at  $1,573\text{ cm}^{-1}$  due to the presence of C–C stretching in graphitic domains of sample S-1. With further increase in oxidation level, the FT-IR spectrum reveal the presence of C=O ( $1,720\text{ cm}^{-1}$ ), C–O ( $1,050\text{ cm}^{-1}$ ), C–O–C ( $1,250\text{ cm}^{-1}$ ), C–OH ( $1,403\text{ cm}^{-1}$ ) in the GO samples. The peak at  $1,620\text{ cm}^{-1}$  is a resonance peak that can be assigned to the C–C stretching and absorbed hydroxyl groups in the GO.

### 2.1.5 Raman

Raman spectroscopy is a non-destructive technique that is widely used to obtain structural information of carbon materials. Usually, the Raman spectrum of a GO film displays a D band at  $\sim 1,350\text{ cm}^{-1}$  and a broad G band at  $\sim 1,580\text{ cm}^{-1}$  [11]. The G peak is the characteristic of all  $\text{sp}^2$ -hybridized carbon networks, which originates from the first-order scattering from the doubly degenerate  $\text{E}_{2g}$  phonon modes of graphite in the Brillouin zone center as well as bond stretching of  $\text{sp}^2$  carbon pairs in both rings and chains. Meanwhile, the D peak is due to the breathing mode of aromatic rings [23], which comes from the structural imperfections created by the attachment of oxygenated groups on the carbon basal plane [19]. Therefore, the D-peak intensity is often used as a measure for the degree of disorder [24]. Generally, the integrated intensity ratio of the D- and G-bands ( $I_D/I_G$ ) indicates the oxidation degree and the size of  $\text{sp}^2$  ring clusters in a  $\text{sp}^3/\text{sp}^2$  hybrid network of carbon atoms. Another peak around  $2,680\text{ cm}^{-1}$ , usually called 2D peak, is the overtone



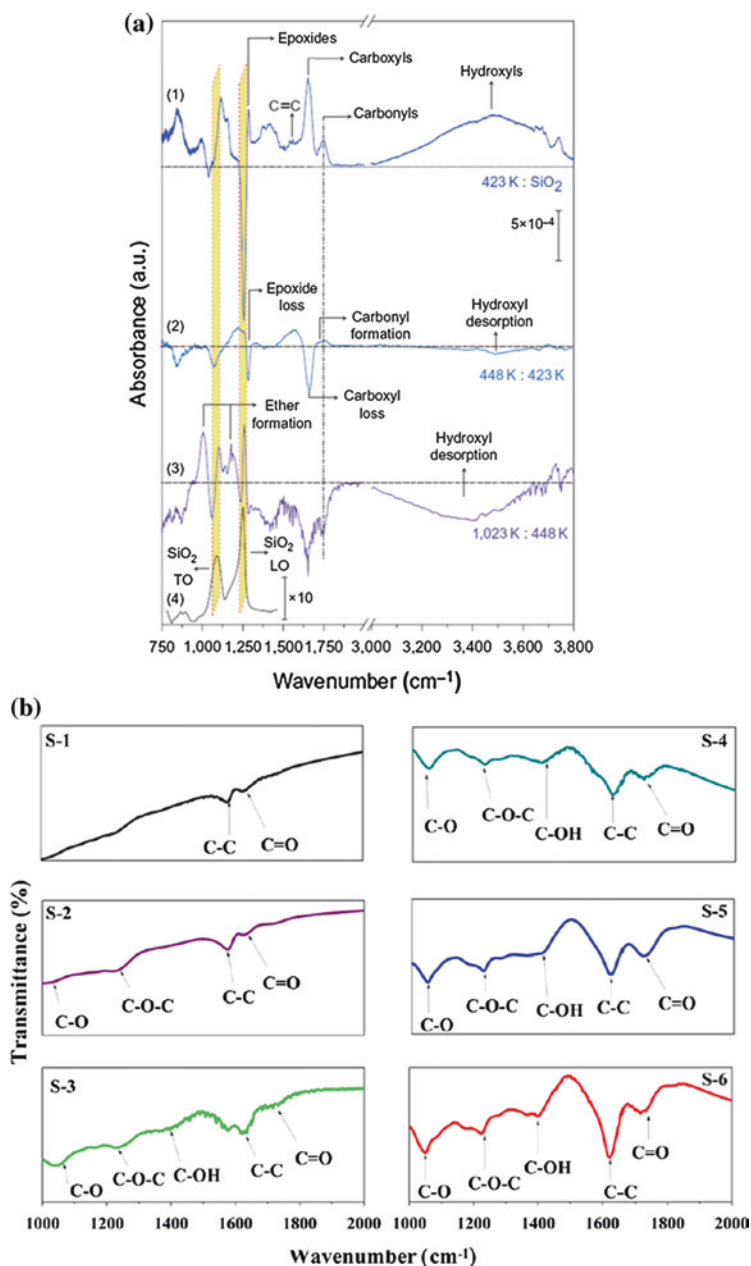
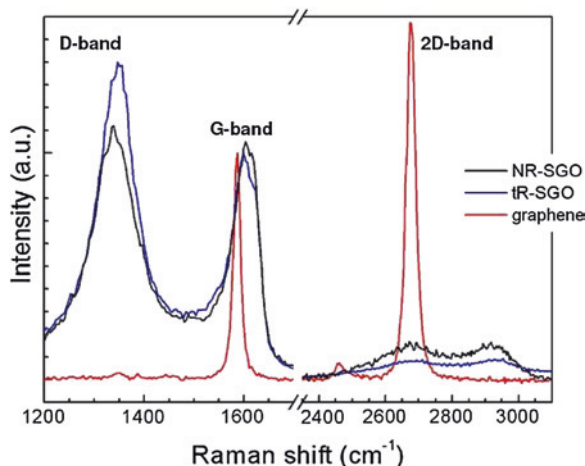


**Fig. 2.4** **a** FT-IR spectra of single-layer GO: annealing at 423 K and referenced to the bare oxidized silicon substrate the spectrum (1); annealing to 448 K (2), referenced to spectrum (1); annealing to 1,023 K (3), referenced to spectrum (2); full SiO<sub>2</sub> absorption of the oxide referenced to H-terminated silica (4). Reprinted with permission from Ref. [15]. Copyright (2010) Nature Publishing Group. **b** FT-IR spectra of GO with different degrees of oxidation from samples S-1 to S-6. Reprinted with permission from Ref. [18]. Copyright (2012) Elsevier Ltd.

**Fig. 2.5** Raman spectra of single-sheet GO (NR-SGO), single-sheet thermally reduced GO (tR-SGO), and mechanically exfoliated single-sheet graphene on SiO<sub>2</sub>/Si substrates normalized to the G-peak intensity. Reprinted with permission from Ref. [28]. Copyright (2008) American Chemical Society



of the D peak, which reflects the number of graphene layers [25, 26]. The 2D peak is attributed to double resonance transitions resulting in production of two phonons with opposite momentum. Different from the D peak, which is only Raman active in the presence of defects, the 2D peak is active even in the absence of any defects [27].

Figure 2.5 compares typical Raman spectra of GO, RGO and graphene, which were recorded at an excitation wavelength of 532 nm [28]. Generally, the Raman spectra of GO and RGO are very close to each other, both exhibiting the same D, G and 2D peak positions. The only distinct difference is the  $I_D/I_G$  ratio since RGO usually has much lower oxidation degree than that of GO. Compared with graphene, the prominent D peak along with weak and broad 2D peak are the main signs of GO due to structural disorder [29]. Usually, the D peak is absent in graphene [30]. Meanwhile, the mechanically exfoliated graphene has a much strong and sharp 2D peak.

Krishnamoorthy et al. [18] studied the Raman spectra of GO with different degrees of oxidation. During oxidation of graphite, the G band is shifted from  $1,570\text{ cm}^{-1}$  (G band of graphite) towards a higher wavenumber ( $1,585\text{ cm}^{-1}$ ) and the D band has higher intensity, which can attributed to the formation of defects and disorder such as the presence of in-plane heteroatoms, grain boundaries, aliphatic chains, and so on. On the other hand, the intensity of the 2D band is diminished after oxidation. Moreover, a new band appears around  $2,950\text{ cm}^{-1}$ , which is denoted as D + G band. The reduction in the intensity of the 2D band is attributed to breaking of stacking order associated with oxidation reaction.

## 2.2 Microscopic Characterization

### 2.2.1 TEM

TEM is a common microscopic technique to feature the atomic structures of nanomaterials. By means of TEM, one can directly image the lattice atoms and



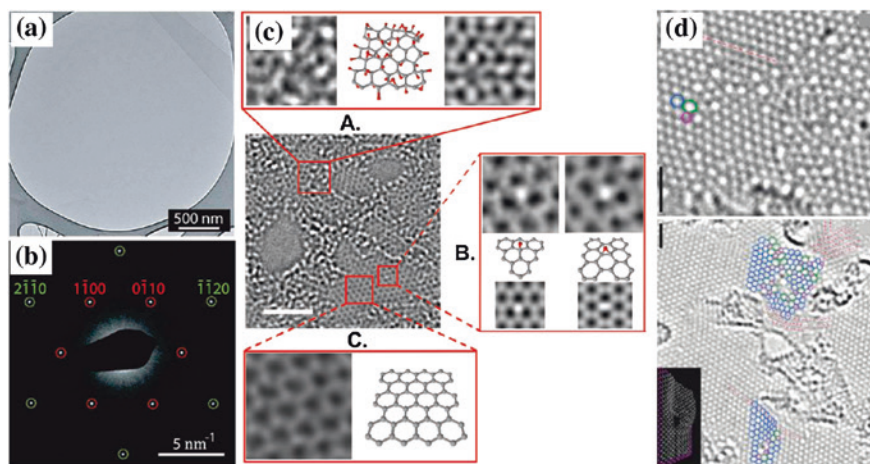


**Fig. 2.6** **a** TEM image of a single GO sheet on a lacey carbon support and **b** its SAED of the center of the region. Reprinted with permission from Ref. [34]. Copyright (2009) American Chemical Society. **c** Aberration-corrected TEM image of a single sheet of suspended GO with a scale bar of 2 nm. Expansion (A) shows, from left to right, a 1 nm<sup>2</sup> enlarged oxidized region of the GO, then a proposed possible atomic structure of this region with carbon atoms in gray and oxygen atoms in red, and finally the average of a simulated TEM image of the proposed structure. Expansion (B) focuses on the white spot on the graphitic region, which moves along the graphitic region. Expansion (C) shows a 1 nm<sup>2</sup> graphitic portion from the planewave reconstruction of a focal series of GO and the atomic structure of this region. Reprinted with permission from Ref. [32]. Copyright (2010) WILEY-VCH Verlag GmbH & Co. KGaA, Weinheim. **d** TEM images of extended topological defects and deformations in RGO, including pentagons, heptagons, distortions and strain in the surrounding lattice. Carbon pentagons, hexagons, and heptagons are indicated in magenta, blue, and green, respectively. The red dashed lines denote directions with strong deformations in the lattice. A relaxed structural model similar to the observed configuration is shown in inset. Reprinted with permission from Ref. [31]. Copyright (2010) American Chemical Society

topological defects in GO [21, 31–33], which is of significant importance to explore their atomic structure. A typical TEM image of a GO monolayer shown in Fig. 2.6a indicates it is highly electron transparent even in comparison to the thin-film carbon support [34]. A selected area electron diffraction (SAED) pattern from the monolayer region of the GO film is shown in Fig. 2.6b. It should be noticed that clear diffraction spots are observed, indicating that the crystalline order of the original graphene lattice is preserved. Meanwhile, for GO samples with different oxidation degrees, their TEM images show different transparencies because of different number of layers in the stacked structure of GO [18]. At lower oxidation degree, the samples contain less oxygenated functional groups which limits them in terms of exfoliation into monolayers or few layers after the exfoliation process. With increasing the oxidation level, GO samples become highly transparent since the samples possess high amounts of oxygenated functional groups and can be easily exfoliated into monolayers or just a few layers of GO after ultrasonic treatment.

High-resolution TEM (HRTEM) is able to directly image the honeycomb lattice along with structural disorder in GO. Using HRTEM, Erickson et al. [32] demonstrated that the specific atomistic features of GO shows three major regions, which are holes, graphitic regions, and highly contrast disordered regions with approximate area percentages of 2, 16, and 82 %, respectively (Fig. 2.6c). It is proposed that the holes in GO are formed by releasing CO and CO<sub>2</sub> during the aggressive oxidation and sheet exfoliation. The graphitic regions are resulted from incomplete oxidation of the basal plane, which preserves the honeycomb structure of graphene. Meanwhile, the disordered regions of the basal plane are originated from abundant oxygen-containing groups aggregated in these regions, including hydroxyls, epoxies, and carbonyls. Gómez-Navarro et al. [31] further unraveled the topological defects in GO using aberration-corrected HRTEM. They pointed out the dominant clustered pentagons and heptagons, as well as the existence of in-plane distortions and strain in the surrounding lattice of GO, as displayed in Fig. 2.6d.

### 2.2.2 STM

Another useful microscopic technique is STM. Previously, several groups have utilized STM to study the surface of GO and observed highly defective regions [35–39]. According to Gómez-Navarro et al.'s measurement [35], pristine graphene and oxidized regions are distinguishable through the bright spots as shown in Fig. 2.7a, where the oxidized regions are marked by green contours. By estimating the ratio of oxidized regions, the degree of functionalization can be obtained. Then, Kudin et al. [36] compared the STM images of highly oriented pyrolytic graphite (HOPG) and GO, as depicted in Fig. 2.7b. The STM image of HOPG is presented in the inset at the left bottom of Fig. 2.7b, which is in a highly crystalline order. In contrast, the STM image of GO appears rough, featuring a peak-to-peak topography of 1 nm. This roughness is caused by functional groups and defects. Fourier transformation of the STM image (inset at the right top of Fig. 2.7b) shows a clear signature of a graphitic backbone where the hexagonal symmetry is highlighted by manually added lines. This indicates reemergence of graphitic order during the reduction process.

Pandey et al. [38] also examined the oxidized regions of GO and surprisingly observed a periodic arrangement of oxygen atoms, which spanned over a few nanometers, as shown in Fig. 2.7c. This periodic arrangement can be understood by a structural model illustrated in Fig. 2.7d, where oxygen atoms are arranged in a rectangular lattice, suggesting a series of epoxy groups are presented in strips.

In addition, through the STM images, Doğan et al. [39] shows the defects of vacancies and adatoms in the electrochemically reduced GO. Particularly, from the atomically resolved STM images obtained at different parts of the same reduced GO sample, they observed a moiré pattern, where the GO sample exhibits

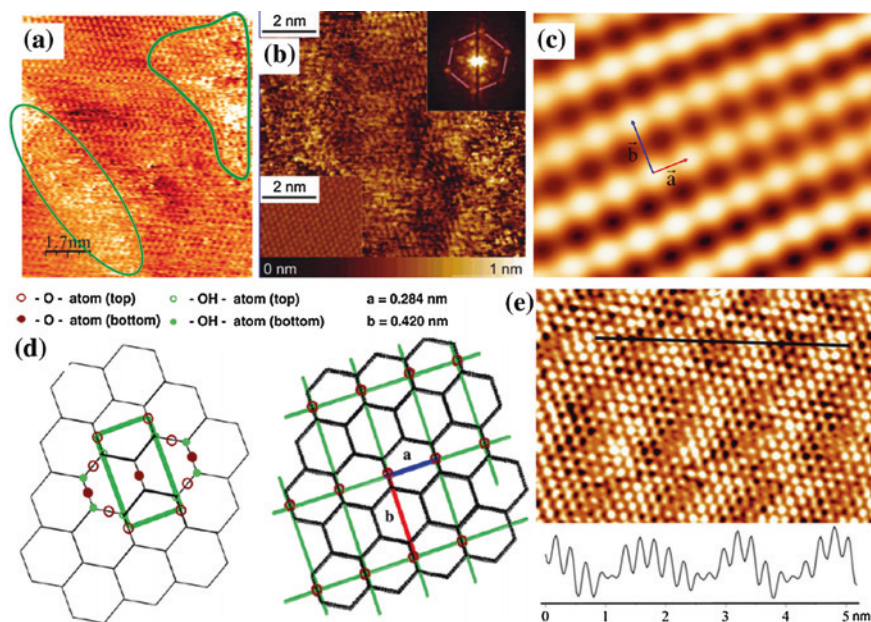


**Fig. 2.7** **a** STM image of a GO monolayer on a HOPG substrate, taken under ambient conditions. Oxidized regions are marked by *green* contours. Reprinted with permission from Ref. [35]. Copyright (2007) American Chemical Society. **b** STM image of a GO monolayer on a HOPG substrate and its Fourier transform (*inset at top right*). Reprinted with permission from Ref. [36]. Copyright (2008) American Chemical Society. **c** High-resolution STM image of the oxidized regions of GO revealing a rectangular lattice of oxygen atoms. **d** A structural model of GO to show the case of (c). Reprinted with permission from Ref. [38]. Copyright (2008) Elsevier B.V. **e** An atomically resolved STM image of the electrochemically reduced GO film showing a Moiré pattern with a periodicity of around 1.45 nm, where the lower part of the figure shows the height profiles taken along the *black line*. Reprinted with permission from Ref. [39]. Copyright (2013) Elsevier B.V.

a hexagonal lattice with an average periodicity of about  $\sim 1.45$  nm, as presented in Fig. 2.7e. This hexagonal moiré structures originate from the lattice mismatch between the graphene and the surface of hexagonally close-packed (hcp) Au solid, which leads to incommensurate structures.

### 2.2.3 Other Microscopic Tools and Combined Techniques

Besides TEM and STM, other microscopic means are also helpful to reveal the atomistic structures of GO. For example, AFM directly gives the apparent thickness as well as the number of layers of GO [6, 35, 37, 38]. Generally, analysis of a larger number of AFM images reveals that GO sheets have lateral dimensions

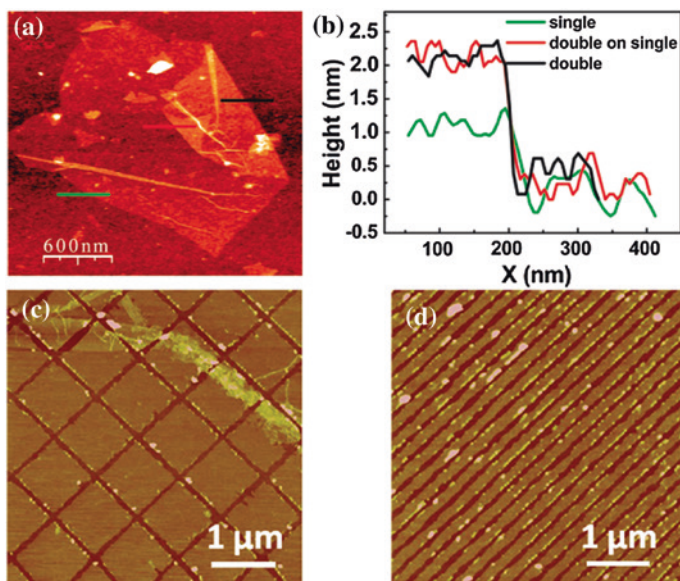


**Fig. 2.8** **a** AFM image of a GO monolayer deposited on a  $\text{SiO}_2$  substrate, showing a back-folded edge; **b** AFM section profiles along the three different lines in panel **(a)**, revealing mono-, bi-, and tri-layer structures, respectively. Reprinted with permission from Ref. [35]. Copyright (2007) American Chemical Society. AFM nanolithography of GO sample into square arrays **(c)** and linear arrays **(d)**. Reprinted with permission from Ref. [41]. Copyright (2010) AIP Publishing LLC

of 100–5,000 nm and heights in the range of 1.1–15 nm. Approximately 80 % of the GO sheets displayed a height of  $1.1 \pm 0.2$  nm. Figure 2.8a displays an AFM image of a GO sheet whose upper right edge is double-folded onto itself, as can be concluded from the cross-sectional profiles depicted in Fig. 2.8b. Meanwhile, AFM can be utilized for nanolithography [40–42], where GO samples can be etched into different shapes, such as squares, ribbons, quantum dots, as shown in Fig. 2.8c–d.

In addition, using high-resolution annular dark field (ADF) imaging in a STEM instrument, Mkhoyan et al. [43] investigated the oxygen distribution on a GO monolayer. Their results indicated that the degree of oxidation fluctuates at nanometer scale, suggesting the presence of  $\text{sp}^2$  and  $\text{sp}^3$  carbon clusters of a few nanometers. Employing STEM combined with electron energy loss spectroscopy (EELS), they were then able to measure the fine structure of the carbon, oxygen K-edges, and low-loss electronic excitations in GO [43]. They found that the oxygen atoms are randomly attached to the graphene sites, converting the  $\text{sp}^2$  carbon in graphene to  $\text{sp}^3$  hybridization.

Also employing the STEM, Zhu et al. [44] analyzed structural changes of GO nanoribbons during thermal annealing, as shown in Fig. 2.9. Usually, the chemical changes of GO nanoribbons are directly related to the planarity and the  $\text{sp}^2$ -carbon



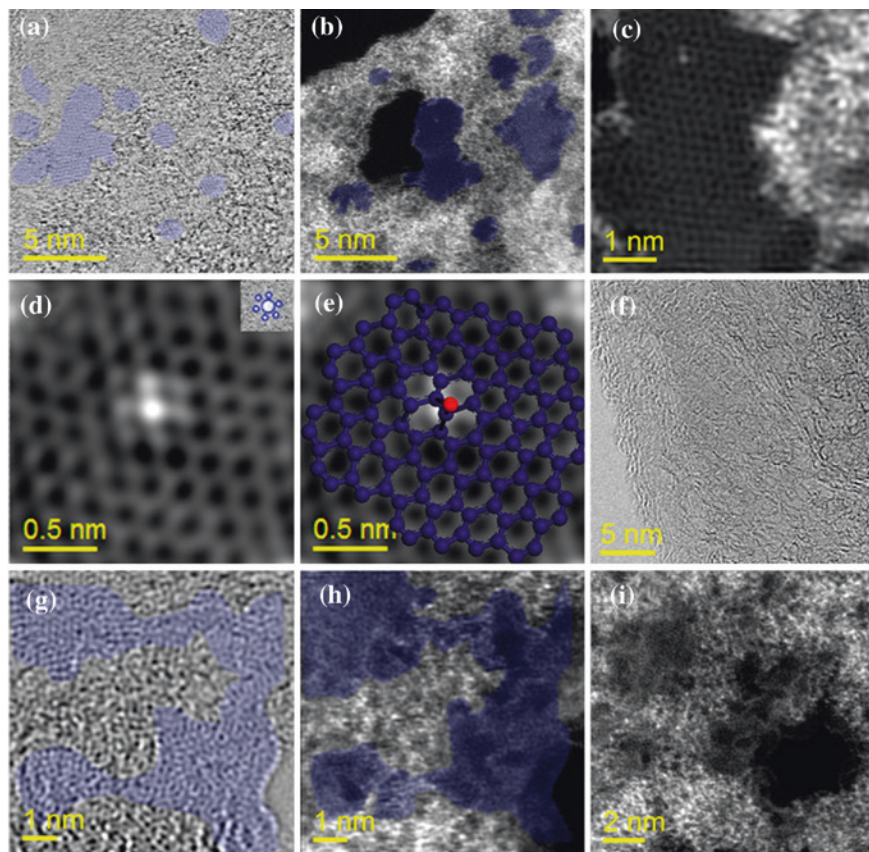


**Fig. 2.9** STEM images of the non-annealed GO nanoribbons (**a–e**) and GO nanoribbons annealed at 200 °C for 10 min (**f–i**). **a** Bright field (BF) and **b** high-angle annular dark-field (HAADF) STEM image of GO nanoribbons with graphene regions shown in blue. **c** HAADF STEM image of a monolayer graphene region (same area as the center in **b**). **d** High-resolution image of monolayer graphene with an oxygen functional group on the basal surface after applying a filter of the raw HAADF STEM image. **e** HAADF STEM image of the same region shown in **(d)** with an overlay structure sketch. **f** BF STEM image of annealed GO nanoribbons with stacked graphene layers. **g** BF STEM image and **h** HAADF STEM image of annealed GO nanoribbons with graphene regions shown in blue. **i** HAADF STEM image of annealed GONRs with holes. Reprinted with permission from Ref. [44]. Copyright (2012) American Chemical Society

structures. As shown in Fig. 2.9a–e, in the non-annealed samples, nanoscale regions of monolayer graphene are observed, where the region sizes typically range from 1 to 2 nm. But in some directions it can be as long as 3–5 nm, as shown in Fig. 2.9a, b. However, the majority of the film is functionalized with oxygen-containing groups, as indicated in Fig. 2.9d, e. Meanwhile, the graphitic regions are small and isolated in a non-annealed sample. During thermal annealing, the structure of GO sample changes, even forming some holes, as indicated by the black regions in Fig. 2.9h, i.

## References

1. He, H., Riedl, T., Lerf, A., Klinowski, J.: *J. Phys. Chem.* **100**, 19954–19958 (1996)
2. Lerf, A., He, H., Riedl, T., Forster, M., Klinowski, J.: *Solid State Ion.* **101–103**, 857–862 (1997)
3. Lerf, A., He, H., Forster, M., Klinowski, J.: *J. Phys. Chem. B* **102**, 4477–4482 (1998)
4. Szabó, T., Berkesi, O., Forgó, P., Josepovits, K., Sanakis, Y., Petridis, D., Dékány, I.: *Chem. Mater.* **18**, 2740–2749 (2006)
5. Cai, W.W., Piner, R.D., Stadermann, F.J., Park, S., Shaibat, M.A., Ishii, Y., Yang, D.X., Velamakanni, A., An, S.J., Stoller, M., An, J.H., Chen, D.M., Ruoff, R.S.: *Science* **321**, 1815–1817 (2008)
6. Stankovich, S., Dikin, D.A., Piner, R.D., Kohlhaas, K.A., Kleinhammes, A., Jia, Y., Wu, Y., Nguyen, S.T., Ruoff, R.S.: *Carbon* **45**, 1558–1565 (2007)
7. Gao, W., Alemany, L.B., Ci, L.J., Ajayan, P.M.: *Nat. Chem.* **1**, 403–408 (2009)
8. Zhang, Q., Scrafford, K., Li, M., Cao, Z., Xia, Z., Ajayan, P.M., Wei, B.: *Nano Lett.* **14**, 1938–1943 (2014)
9. Casabianca, L.B., Shaibat, M.A., Cai, W.W., Park, S., Piner, R., Ruoff, R.S., Ishii, Y.: *J. Am. Chem. Soc.* **132**, 5672–5676 (2010)
10. Mattevi, C., Eda, G., Agnoli, S., Miller, S., Mkhoyan, K.A., Celik, O., Mastrogiorganni, D., Granozzi, G., Garfunkel, E., Chhowalla, M.: *Adv. Funct. Mater.* **19**, 2577–2583 (2009)
11. Yang, D., Velamakanni, A., Bozoklu, G., Park, S., Stoller, M., Piner, R.D., Stankovich, S., Jung, I., Field, D.A., Ventrice, C.A., Ruoff, R.S.: *Carbon* **47**, 145–152 (2009)
12. Akhavan, O.: *Carbon* **48**, 509–519 (2010)
13. Ganguly, A., Sharma, S., Papakonstantinou, P., Hamilton, J.: *J. Phys. Chem. C* **115**, 17009–17019 (2011)
14. Lahaye, R.J.W.E., Jeong, H.K., Park, C.Y., Lee, Y.H.: *Phys. Rev. B* **79**, 125435 (2009)
15. Bagri, A., Mattevi, C., Acik, M., Chabal, Y.J., Chhowalla, M., Shenoy, V.B.: *Nat. Chem.* **2**, 581–587 (2010)
16. Hontoria-Lucas, C., López-Peinado, A.J., López-González, JdD, Rojas-Cervantes, M.L., Martín-Aranda, R.M.: *Carbon* **33**, 1585–1592 (1995)
17. Schniepp, H.C., Li, J.L., McAllister, M.J., Sai, H., Herrera-Alonso, M., Adamson, D.H., Prud'homme, R.K., Car, R., Saville, D.A., Aksay, I.A.: *J. Phys. Chem. B* **110**, 8535–8539 (2006)
18. Krishnamoorthy, K., Veerapandian, M., Yun, K., Kim, S.J.: *Carbon* **53**, 38–49 (2013)
19. Chen, D., Feng, H., Li, J.: *Chem. Rev.* **112**, 6027–6053 (2012)
20. Saxena, S., Tyson, T.A., Negusse, E.: *J. Phys. Chem. Lett.* **1**, 3433–3437 (2010)
21. Pacilé, D., Meyer, J.C., Fraile Rodríguez, A., Papagno, M., Gómez-Navarro, C., Sundaram, R.S., Burghard, M., Kern, K., Carbone, C., Kaiser, U.: *Carbon* **49**, 966–972 (2011)
22. Lee, D.W., De Los Santos, V.L., Seo, J.W., Felix, L.L., Bustamante, D.A., Cole, J.M., Barnes, C.H.W.: *J. Phys. Chem. B* **114**, 5723–5728 (2010)
23. Tuinstra, F., Koenig, J.L.: *J. Chem. Phys.* **53**, 1126–1130 (2003)
24. Ferrari, A.C., Robertson, J.: *Phys. Rev. B* **61**, 14095 (2000)
25. Ferrari, A.C., Meyer, J.C., Scardaci, V., Casiraghi, C., Lazzeri, M., Mauri, F., Piscanec, S., Jiang, D., Novoselov, K.S., Roth, S.: *Phys. Rev. Lett.* **97**, 187401 (2006)
26. Gupta, A., Chen, G., Joshi, P., Tadigadapa, S., Eklund, P.C.: *Nano Lett.* **6**, 2667–2673 (2006)
27. Eda, G., Chhowalla, M.: *Adv. Mater.* **22**, 2392–2415 (2010)
28. Jung, I., Dikin, D.A., Piner, R.D., Ruoff, R.S.: *Nano Lett.* **8**, 4283–4287 (2008)
29. Robinson, J.A., Wetherington, M., Tedesco, J.L., Campbell, P.M., Weng, X., Stitt, J., Fanton, M.A., Frantz, E., Snyder, D., VanMil, B.L.: *Nano Lett.* **9**, 2873–2876 (2009)
30. Malard, L.M., Pimenta, M.A., Dresselhaus, G., Dresselhaus, M.S.: *Phys. Rep.* **473**, 51–87 (2009)
31. Gómez-Navarro, C., Meyer, J.C., Sundaram, R.S., Chuvilin, A., Kurasch, S., Burghard, M., Kern, K., Kaiser, U.: *Nano Lett.* **10**, 1144–1148 (2010)



32. Erickson, K., Erni, R., Lee, Z., Alem, N., Gannett, W., Zettl, A.: *Adv. Mater.* **22**, 4467–4472 (2010)
33. Xie, J., Tu, F., Su, Q., Du, G., Zhang, S., Zhu, T., Cao, G., Zhao, X.: *Nano Energy* **5**, 122–131 (2014)
34. Wilson, N.R., Pandey, P.A., Beanland, R., Young, R.J., Kinloch, I.A., Gong, L., Liu, Z., Suenaga, K., Rourke, J.P., York, S.J.: *ACS Nano* **3**, 2547–2556 (2009)
35. Gómez-Navarro, C., Weitz, R.T., Bittner, A.M., Scolari, M., Mews, A., Burghard, M., Kern, K.: *Nano Lett.* **7**, 3499–3503 (2007)
36. Kudin, K.N., Ozbas, B., Schniepp, H.C., Prud'homme, R.K., Aksay, I.A., Car, R.: *Nano Lett.* **8**, 36–41 (2008)
37. Paredes, J.I., Villar-Rodil, S., Solis-Fernandez, P., Martinez-Alonso, A., Tascon, J.M.D.: *Langmuir* **25**, 5957–5968 (2009)
38. Pandey, D., Reifengerger, R., Piner, R.: *Surf. Sci.* **602**, 1607–1613 (2008)
39. Doğan, H.Ö., Ekinici, D., Demir, Ü.: *Surf. Sci.* **611**, 54–59 (2013)
40. Masubuchi, S., Ono, M., Yoshida, K., Hirakawa, K., Machida, T.: *Appl. Phys. Lett.* **94**, 082107 (2009)
41. He, Y., Dong, H., Li, T., Wang, C., Shao, W., Zhang, Y., Jiang, L., Hu, W.: *Appl. Phys. Lett.* **97**, 133301 (2010)
42. Lu, G., Zhou, X., Li, H., Yin, Z., Li, B., Huang, L., Boey, F., Zhang, H.: *Langmuir* **26**, 6164–6166 (2010)
43. Mkhoyan, K.A., Contryman, A.W., Silcox, J., Stewart, D.A., Eda, G., Mattevi, C., Miller, S., Chhowalla, M.: *Nano Lett.* **9**, 1058–1063 (2009)
44. Zhu, Y., Li, X., Cai, Q., Sun, Z., Casillas, G., Jose-Yacaman, M., Verduzco, R., Tour, J.M.: *J. Am. Chem. Soc.* **134**, 11774–11780 (2012)

Graphene Oxide: Physics and Applications

Zhao, J.; Liu, L.; Li, F.

2015, XIII, 154 p. 81 illus., 45 illus. in color., Softcover

ISBN: 978-3-662-44828-1